Int J Adv Manuf Technol (2017) 90:3567–3574
DOI 10.1007/s00170-016-9632-y

ORIGINAL ARTICLE

Finite element modeling of grain growth by point tracking method in friction stir welding of AA6082-T6

Z. Y. Wan [1] · Z. Zhang [1] · X. Zhou [1]

Received: 15 March 2016 / Accepted: 17 October 2016 / Published online: 11 November 2016

Abstract A thermo-mechanical re-meshing model of friction stir welding (FSW) process of AA6082-T6 is used with a point tracking method for the determination of the final locations of the particles. The relations between the field variables and the material flows in the FSW process are discussed. Then the grain sizes after recrystallization are calculated. The comparison with the numerical and the experimental results in published literatures shows the validity of the proposed model. Based on the Zener-Hollomon parameter, the effects of strain rate and temperature on recrystallization are further discussed.

Keywords Friction stir welding · Coupled thermo-mechanical model · Material flow · Grain size

1 Introduction

As a solid joining process, friction stir welding (FSW) was originally invented in 1991 [1]. In the FSW process, the welding tool consisting of a shoulder and a pin is inserted into the welding plates. By friction and plastic deformation, the welding plates can be heated and becomes softer to ensure the success of the welding. FSW has been identified as a thermo-mechanical [2] and hot working process [3]. The material around the welding tool can be stirred and flows [4]. Frigaard et al. [5] developed a numerical model of a moving 3D heat source model and compared the calculated temperature with the measured data. Hamilton et al. [6] presented a thermal model that utilizes a slip factor of new energy based on the maximum welding temperature to solidus temperature ratio. Zhang and Zhang [7] presented a thermo-mechanical model and indicated that the material flow was affected extensively by the tool shoulder near the top surface. Buffa et al. [8] and Fratini et al. [9] proposed 3D finite element re-meshing models for simulation of temperature variations and for prediction of grain sizes in friction stir welding. Đurđević et al. [10] simulated the fatigue crack growth in friction stir welding based on XFEM. Kadian et al. [11] used laminar and turbulent models to study the material flows in friction stir welding. Asadi et al. [12] proposed 3D models using the software package to investigate friction stir welding of magnesium alloys. Ghetiya et al. [13] predicted the temperature rises in immersed friction stir welding and found that the peak temperature area becomes narrower. Chansoria et al. [14] studied the effect of welding parameters on transient temperature distributions in friction stir welding of steel. The residual stress occurs due to the non-uniform simultaneous heating and cooling [15]. By the use of sequentially coupled model, Riahi et al. [16] found that the heat distribution along the weld thickness varies and is asymmetrical enormously based on the predicted residual stresses.

As mentioned above, FSW has been recognized as a kind of hot working deformation process due to its large deformation. The welding temperature is usually greater than $0.6T_m$. So, in the perspective of hot working process, normally, two metallurgy factors (temperature rise and material deformation) make the main contribution to the grain annihilation and to the formation of the new microstructure. This process involves a combination of recovery and recrystallization. Commonly, dynamic recovery and recrystallization can be considered as reasons for the decrease of the flow stress of the weld material [17, 18].

✉ Z. Zhang
zhangz@dlut.edu.cn

[1] Department of Engineering Mechanics, State Key Laboratory of Structural Analysis for Industrial Equipment, Faculty of Vehicle Engineering and Mechanics, Dalian University of Technology, Dalian 116024, China

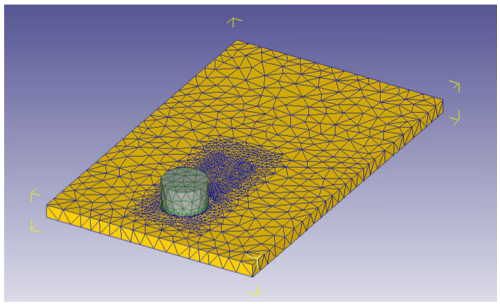

Fig. 1 The configuration of the FE model

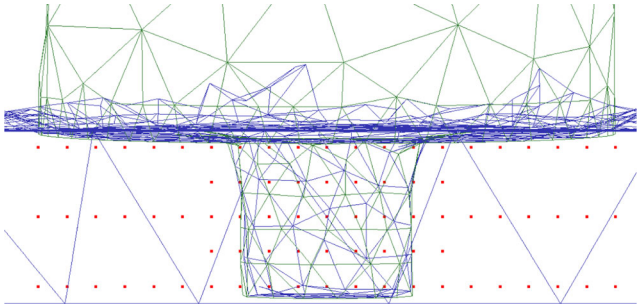

Fig. 3 Preliminary locations of traced material particles

Zhang et al. [19] developed a 2D model based on solid mechanics and showed that the material at the advancing side rotates with the pin for several revolutions, whereas the material at the retreating side experiences no rotation around the pin. Schmidt and Hattel [20] showed that the rotation speed is the main factor for the determination of the temperature rise and material flow. Higher rotation speed can lead to more localized deformation near the tool surface [21]. By the use of Taguchi method, the welding parameters can be optimized [22].

The material flow and the temperature rises in FSW have been studied by many researchers. Both the two factors can affect the final grain sizes after the recrystallization process in FSW. Fratini et al. [9] proposed a recrystallization formula for the calculation of the final grain size in a re-meshing finite element model of FSW. Arora et al. [23] simulated the temperature distribution and estimated the grain size during friction stir welding by using finite difference equations. Based on a ALE model and the Zener-Hollomon parameter, Zhang and Wu [24] calculated the final grain sizes with different tool diameters. The cellular automata method [25] and Monte Carlo method [26] can be also used for the simulations of grain growth in FSW.

However, the differences about final locations of the flowing points with consideration of the grain growth have not been clearly investigated. So, a 3D Lagrangian thermo-mechanical coupled incremental finite element (FE) model of the FSW is developed in current work. Material flow is visualized using the point tracking method to locate the final positions of the flowing points. The final grain sizes in the final locations of the traced points can be then calculated by the temperature and strain rate histories extracted from the FE model. The obtained results are compared to the experimental data in the published literature for the validation of the proposed method.

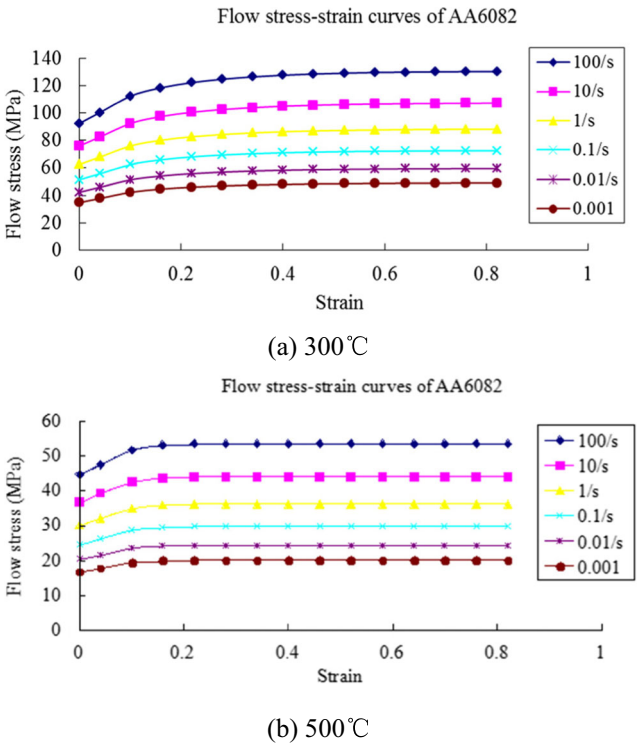

Fig. 2 Flow stress-strain curves in different strain rates for AA6082-T6

2 Model description

The configuration of the FE model can be seen in Fig. 1. It consists of two components: a tool and a workpiece. The size of the workpiece is 80 mm × 50 mm × 3 mm. A cylindrical smooth pin is used in this work. The pin height is 2.8 mm. The pin diameter is 3 mm and the shoulder diameter is 10 mm.

The FSW process can be divided into the plunging stage and the welding stage. So, FSW model should be developed including both the initial state and the following steady state. During the plunging stage in this model, the tool is inserted into the welding plate at 0.1 mm/s with a given rotating speed. Then, the rotating tool with the tilt angle of 2° moves along the

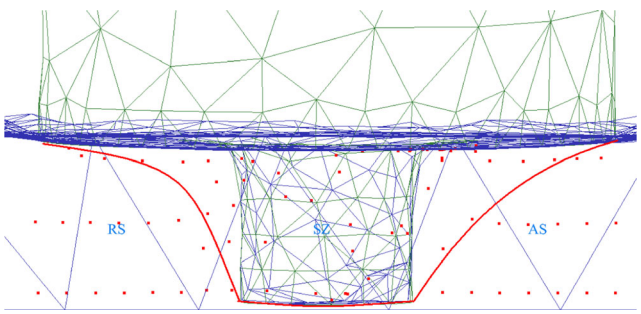

Fig. 4 The final location of traced material particles

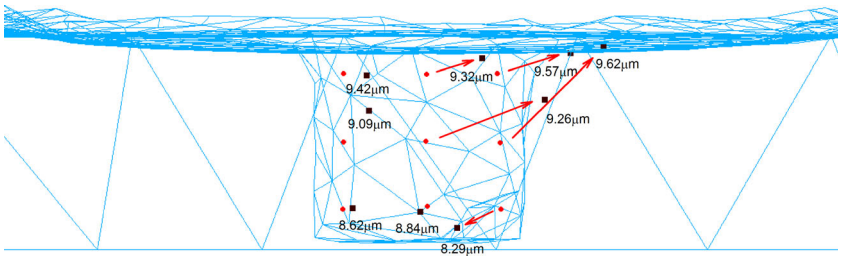

Fig. 5 Grain sizes of flowing particles (71.5 mm/min, 715 rpm)

welding center line during the welding stage. In the plunging stage, the welding plate can be preheated due to the frictional effect of the rotation of the welding tool. The preheating in the plunging stage is one of the main factors to determine the success of FSW [27]. Preheating can be also useful for the improvement of mechanical properties of friction stir weld [28].

The mesh size near the welding tool is set to be 0.75 mm and the mesh size in other regions is set to be 1.5 mm. Re-meshing technique is used to avoid mesh entanglements and excessive distortions. The error of the finite element solution in energy norm can be written as,

$$\|e\|_{\text{all}} = \eta_{\text{all}} \left(\frac{\|U\|^2 + \|e\|^2}{m} \right)^{1/2} \tag{1}$$

where m represents the evolved elements in the re-meshing.

$$\|U\|^2 = \sum_{i=1}^{m} \int \{\varepsilon\}_i^{\mathrm{T}} [E] \{\varepsilon\}_i dV \tag{2}$$

$$\|e\|^2 = \sum_{i=1}^{m} \int \left(\{\varepsilon^*\}_i - \{\varepsilon\}_i \right)^{\mathrm{T}} [E] \left(\{\varepsilon^*\}_i - \{\varepsilon\}_i \right) dV \tag{3}$$

where $\{\varepsilon\}$ is the strain and $[E]$ is the elastic matrix.

In a specified element,

$$\xi_i = \frac{\|e\|_i}{\|e\|_{\text{all}}} \tag{4}$$

The new element size in the re-meshing should be defined as,

$$(h_i)_{\text{new}} = \frac{(h_i)_{\text{old}}}{\xi_i^{\alpha}} \tag{5}$$

where the value of α is determined by the relative location to the singular point. Detailed information on h refinement, p refinement, and h-p refinement can be found in Ref. [29].

The material of the workpiece is AA6082-T6. Figure 2 shows the flow stress curves of the welding material at 300 and 500 °C. The heat capacity is 900 J/Kg·°C. The convection coefficient is 20,000 W/m^2·°C. The thermal conductivity is 180 W/m·°C. The tool material is H13 and the tool is considered as a rigid body.

The constant shear friction model is selected and the friction force is defined by

$$f = mk \tag{6}$$

where f denotes the frictional stress, k the shear yield strength, and m the friction factor. In this research, shear friction factor of 0.6 is used [9].

The temperature in the workpiece can be increased with the increase of the plastic deformation. It is assumed that heat generation in the deformation zone is attributed to plastic deformation and frictional work at the tool-workpiece interface,

$$\dot{r} = \alpha \bar{\sigma} \dot{\varepsilon} \tag{7}$$

where $\dot{r}$ is the heat generation rate, $\bar{\sigma}$ the equivalent stress, and $\dot{\varepsilon}$ the effective strain rate. The factor α represents the mechanical work converted into heat, which is assumed to be 0.9.

In current model, the ambient temperature is selected to be 20 °C. The convection coefficient between the workpiece and the atmosphere is 20 W/m^2·°C. The bottom surface of the workpiece is fixed.

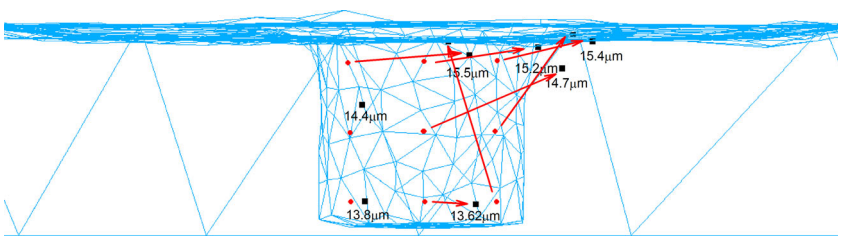

Fig. 6 Grain sizes of flowing particles (100 mm/min, 1000 rpm)

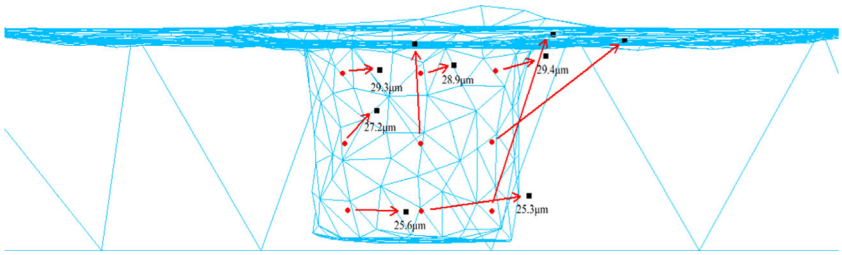

Fig. 7 Grain sizes of flowing particles (100 mm/min, 1500 rpm)

The final grain size can be calculated by the Zener-Hollomon parameter,

$$\log\left(\frac{d}{D}\right) = a + b\log Z \tag{8}$$

where a and b are constants and are selected to be 1.81 and −0.23, respectively. D is the initial grain size and is 80 μm. Z is the Zener-Hollomon parameter,

$$Z = \dot{\bar{\varepsilon}} \exp\left(\frac{Q}{RT}\right) \tag{9}$$

where $\dot{\bar{\varepsilon}}$ is the equivalent strain rate, Q (180 kJ/mol) is the material activation energy, R is the gas constant, and T is the absolute temperature.

3 Results and discussion

To simulate the material flow phenomenon, point tracking technique is used to track the material particle movements in this work. Figure 3 shows the preliminary locations of the investigated points in the FSW process. The final positions of all the tracking points in Fig. 3 are presented in Fig. 4. The red line in Fig. 4 indicate the boundary for the stirring zone.

The obtained grain sizes on the cross section from the numerical model are shown in Fig. 5. The square particles show the predicted grain sizes of flowing material particles and their final locations. The round points show the initial locations of the traced particles. The predicted grain sizes vary from 9.32 to 9.62 μm near the top surface and from 8.29 to 8.84 μm near the bottom surface. From Ref. [9], the grain

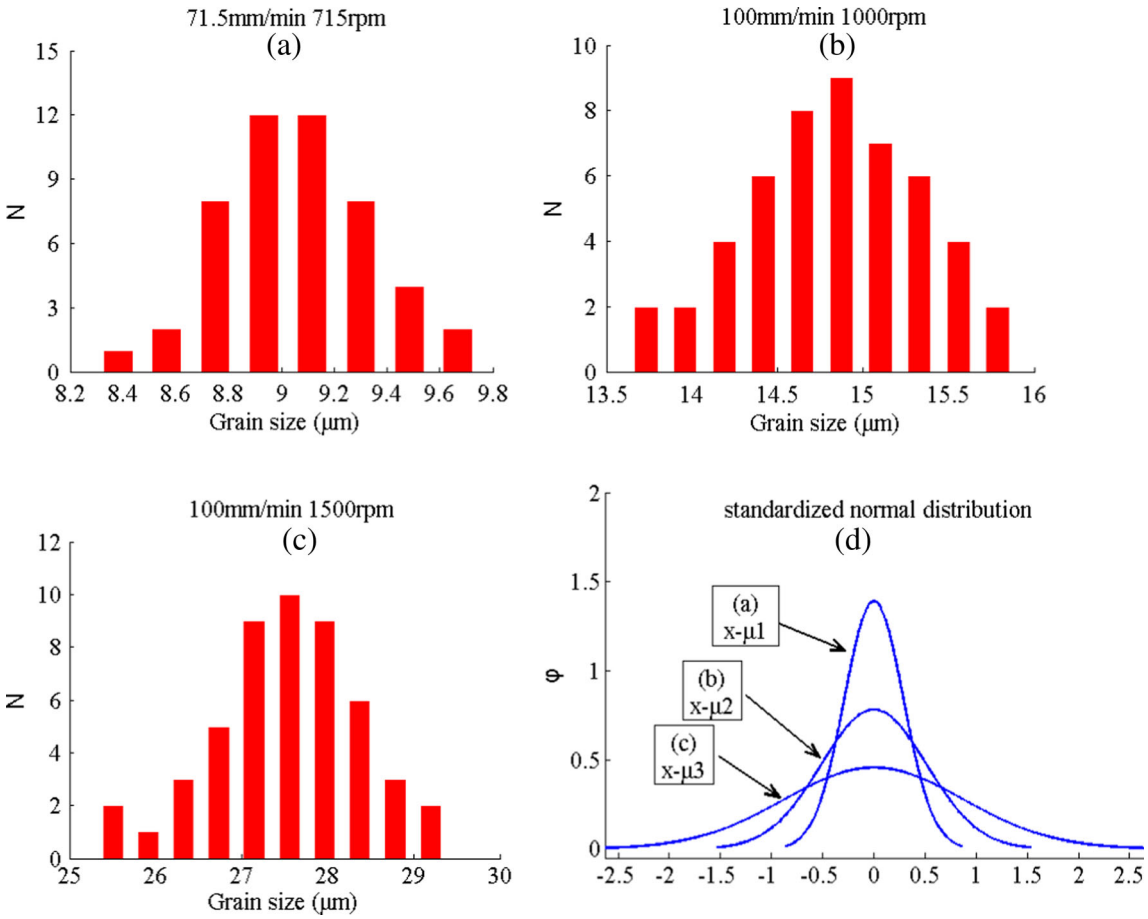

Fig. 8 Statistical grain sizes and probability density functions in different welding conditions

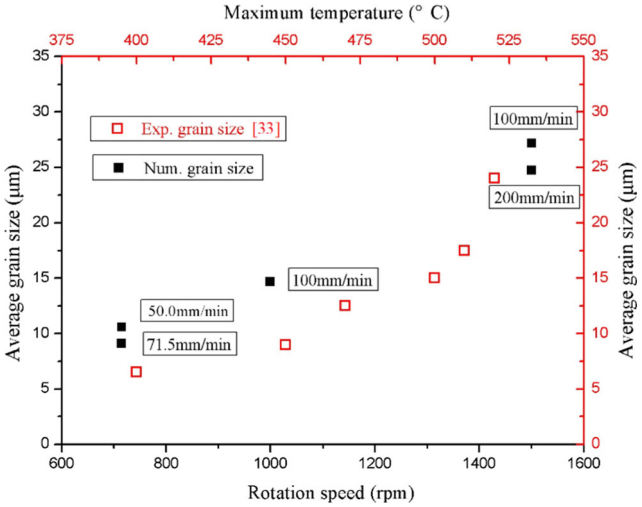

Fig. 9 Relationship between the average grain size and rotation speed

sizes measured on the top surface and the bottom surface are about 11 and 9 μm, respectively. The comparison shows the validity of the current model.

When the transverse speed is increased to 100 mm/min, two cases with different rotating speeds are selected for comparison. The obtained grain sizes on the cross section in 1000 and 1500 rpm are shown in Figs. 6 and 7. It can be clearly seen that some of the material particles are stretched toward the advancing side and can cluster at the advancing side on the top surface. This phenomenon agrees well with the observation of asymmetrical deformation on the cross section [30, 31]. With the increase of the rotating speeds, the average grain sizes on both the top and bottom surfaces are increased.

Fifty material particles in each case inside the stirring zone are selected. By analyzing these grain sizes statistically from different welding conditions, the statistical information of the grain sizes can be obtained, as shown in Fig. 8. It is clearly shown in Fig. 8a–c the mean value of the grain size can be increased with the increase of the rotation speed. The mean value is increased from 9.11 μm in 715 rpm to 27.5 μm in 1500 rpm. Figure 8d shows the probability density functions for the three cases with different welding conditions in standardized normal distribution regardless of each different mean value. The standard deviation varies from 0.287 (a) to 0.5109 (b) to 0.876 (c) as the rotation speed increases. This also means that more similar grain sizes can be found in the direction of weld thickness, which can lead to closer hardness distribution in lower rotating speed. This phenomenon has been observed by experiment [32]. Compared with the cooling of the welding thermal cycle for the particles under the welding condition (a), the cooling periods for material particles shown in Fig. 8b, c become longer and the welding temperatures become higher. The particles with longer cooling period have experienced longer recovery and grain growth after recrystallization, and the variations of the grain sizes on the cross section are increased.

The relationship between the rotation speed of the tool and the grain size is shown in Fig. 9. The average grain size increases with the increase of the rotation speed. This phenomenon can be validated by experiment [33].

Figures 10, 11, and 12 show the temperature and strain rate histories in 715 rpm and 71.5 mm/min. Nine material particles are uniformly positioned in three columns from left to right. At the welding center line, Fig. 10 indicates that particles (P1-P3) have experienced the similar temperature histories due to the similar flowing movement patterns. Semicircular movements from the leading side toward the trailing side can be

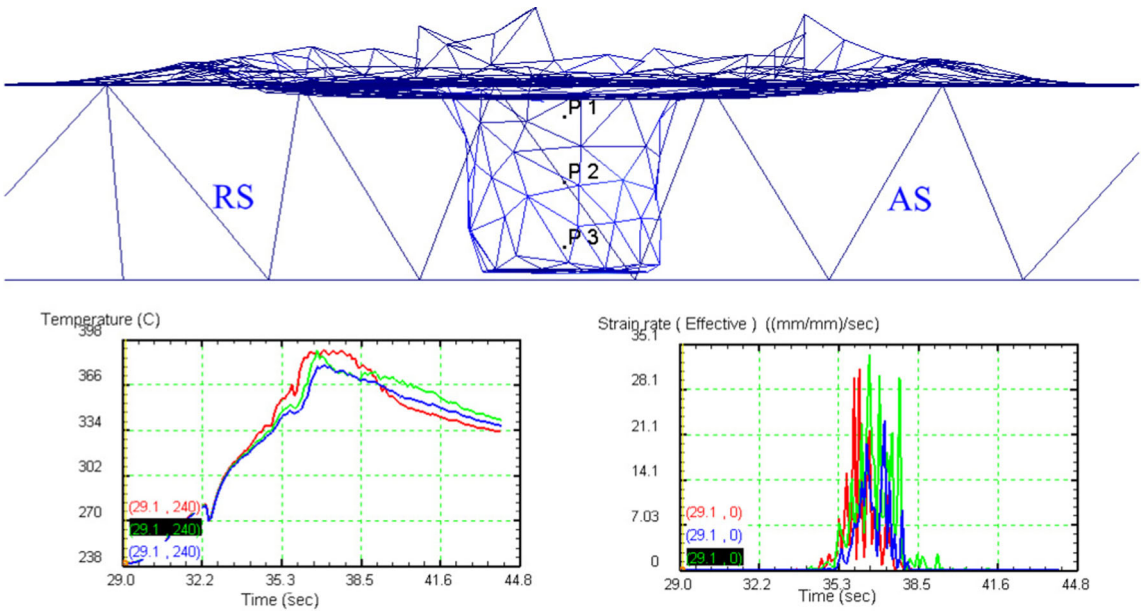

Fig. 10 Temperature and strain rate histories of material particles at weld line

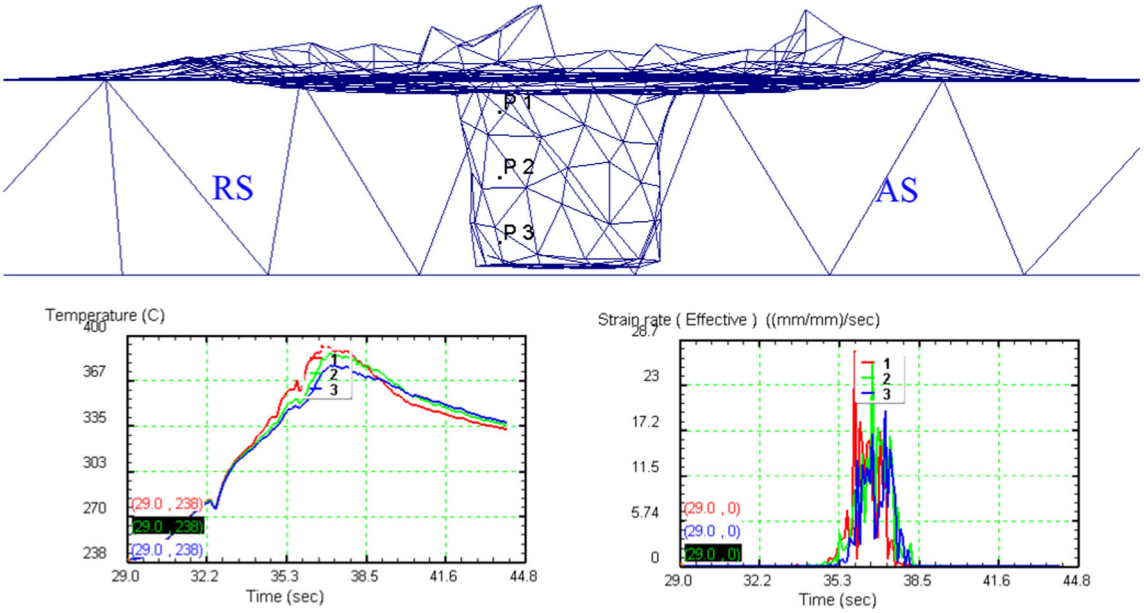

Fig. 11 Temperature and strain rate histories of material particles at retreating side

found for the particles on the center line due to the stirring actions. Figure 11 shows the histories of the three particles initially located at the retreating side. Both the temperature and the strain rate near the bottom surface are lower than the top surface. The histories of the selected three particles at the advancing side can be seen in Fig. 12. In comparison with Fig. 11, the cooling temperature at the advancing side is obviously higher than the retreating side due to the entanglement of the material particles at the advancing side, i.e., the cooling rate of the particles at the advancing side becomes smaller. Detailed information on material flow rules can be found in previous works [3, 7, 34]. The stain rate at the advancing side is obviously higher than the retreating side due to different flow patterns. It can be seen from Figs. 10, 11, and 12 that the peak temperatures of all the traced particles are above 375 °C, which is high enough for recrystallization. The strain rates of particles near the top surface are commonly higher than those near the bottom surface. The strain rates of the particles at the advancing side are slightly higher than the retreating side. In spite of the substantial changes in the strain rate history, the maximum temperature plays a sensitive role in the prediction of the final grain size. As seen from Figs. 10 and 11, the temperature of P1 (top) is about 10–12 °C higher than P3 (bottom). The grain sizes calculated near the top surface of

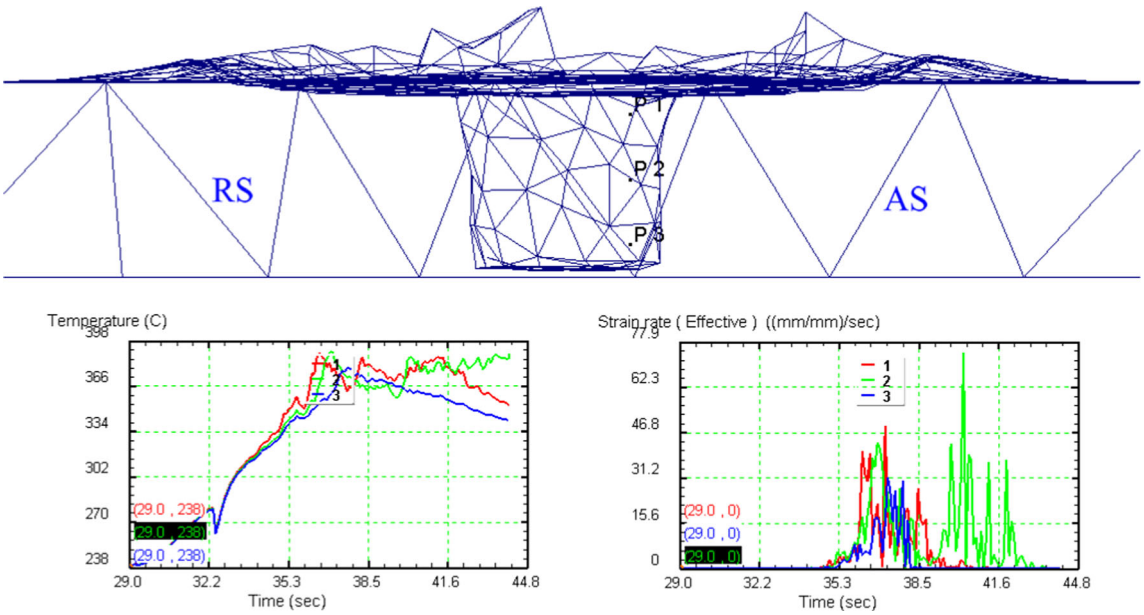

Fig. 12 Temperature and strain rate histories of material particles at advancing side

SZ are slightly larger than that of the bottom due to the temperature differences between the top and bottom surfaces. Commonly, the top slice undergoes a higher temperature thermal cycle and longer cooling time in comparison with the bottom one. This may be the reason for larger grains near the top surface. This means the hardness near the top surface would be lower than that from the bottom due to the different grain sizes, which can be proved by the experimental test [35].

4 Conclusions

A 3D simulation based on the Lagrangian incremental formulations for FSW of AA6082 was developed to track the movements of the material particles. The strain rates and temperature histories of the traced particles are used to calculate the grain sizes on the cross section of the friction stir weld. The obtained results are summarized as follows:

1. The movement of the material particles can clearly show the region of the stirring zone. The material particles in the middle of the weld can move upward and finally are clustered at the advancing side on the top surface.
2. By statistical analysis, both the mean value of the grain size and the standard deviation of the grain size are increased with the increase of the rotating speed.
3. The grain size near the top surface is higher than the bottom surface due to higher temperature and longer cooling process.
4. The stain rate at advancing side is higher than retreating side due to different material flow patterns.

Acknowledgment This work was supported by the Program for New Century Excellent Talents in University, the Fundamental Research Funds for the Central Universities, the National Natural Science Foundation of China (Nos. 11172057 and 11572074), and the National Key Basic Research Special Foundation of China (2011CB013401).

References

1. Mishra RS, Ma ZY (2005) Friction stir welding and processing. Mater Sci Eng R 50:1–78
2. Cederqvist L, Reynolds AP (2001) Factors affecting the properties of friction stir welded aluminum lap joints. Weld J 80(12):281–287
3. Zhang Z, Chen JT (2012) Computational investigations on reliable finite element based thermo-mechanical coupled simulations of friction stir welding. Int J Adv Manuf Technol 60:959–975
4. Guerra M, Schmidt C, McClure JC, Murr LE, Nunes AC (2002) Flow patterns during friction stir welding. Mater Charact 49(2):95–101
5. Frigaard Ø, Grong Ø, Midling OT (2001) A process model for friction stir welding of age hardening aluminum alloys. Metall Mater Trans A 32(5):1189–1200
6. Hamilton C, Dymek S, Sommers A (2008) A thermal model of friction stir welding in aluminum alloys. Int J Mach Tool Manu 48(10):1120–1130
7. Zhang Z, Zhang HW (2009) Numerical studies on controlling of process parameters in friction stir *welding*. J Mater Process Technol 209(1):241–270
8. Buffa G, Hua J, Shivpuri R, Fratini L (2006) Design of the friction stir welding tool using the continuum based FEM model. Mater Sci Eng A 419(1):381–388
9. Fratini L, Buffa G (2005) CDRX modelling in friction stir welding of aluminium alloys. Int J Mach Tool Manu 45(10):1188–1194
10. Đurđević A, Živojinović D, Grbović A, Sedmak A, Rakin M, Dascau H, Kirin S (2015) Numerical simulation of fatigue crack propagation in friction stir welded joint made of Al 2024-T351 *alloy*. Eng Fail Anal 58:477–484
11. Kadian AK, Biswas P (2015) A comparative study of material flow behavior in friction stir welding using laminar and turbulent models. J Mater Eng Perform 24(10):4119–4127
12. Asadi P, Mahdavinejad RA, Tutunchilar S (2011) Simulation and experimental investigation of FSP of AZ91 magnesium alloy. Mater Sci Eng A 528(21):6469–6477
13. Ghetiya ND, Patel KM, Patel AB (2015) Prediction of temperature at weldline in air and immersed friction stir welding and its experimental validation. Int J Adv Manuf Technol 79:1239–1246
14. Chansoria P, Solanki P, Dasgupta MS (2015) Parametric study of transient temperature distribution in FSW of 304 L stainless steel. Int J Adv Manuf Technol 80:1223–1239
15. De A, DebRoy T (2011) A perspective on residual stresses in welding. Sci Technol Weld Join 16:204–208
16. Riahi M, Nazari H (2011) Analysis of transient temperature and residual thermal stresses in friction stir welding of aluminum alloy 6061-T6 via numerical simulation. Int J Adv Manuf Technol 55:143–152
17. Fonda RW, Knipling KE, Bingert JF (2008) Microstructural evolution ahead of the tool in aluminum friction stir welds. Scr Mater 58(5):343–348
18. Prangnell PB, Heason CP (2005) Grain structure formation during friction stir welding observed by the 'stop action technique'. Acta Mater 53(11):3179–3192
19. Zhang HW, Zhang Z, Chen JT (2005) The finite element simulation of the friction stir welding process. Mater Sci Eng A 403(1):340–348
20. Schmidt H, Hattel J (2005) Modelling heat flow around tool probe in friction stir welding. Sci Technol Weld Join 10(2):176–186
21. Colegrove PA, Shercliff HR, Zettler R (2007) Model for predicting heat generation and temperature in friction stir welding from the material properties. Sci Technol Weld Join 12(4):284–297
22. Mohamed MA, Manurung YHP, Berhan MN (2015) Model development for mechanical properties and weld quality class of friction stir welding using multi-objective Taguchi method and response surface methodology. J Mech Sci Technol 29(6):2323–2331
23. Arora HS, Singh H, Dhindaw BK (2012) Numerical simulation of temperature distribution using finite difference equations and estimation of the grain size during friction stir processing. Mater Sci Eng A 543:231–242
24. Zhang Z, Wu Q (2015) Numerical studies of tool diameter on strain rates, temperature rises and grain sizes in friction stir welding. J Mech Sci Technol 29(10):4121–4128
25. Saluja RS, Narayanan RG, Das S (2012) Cellular automata finite element (CAFE) model to predict the forming of friction stir welded blanks. Comput Mater Sci 58:87–100
26. Zhang Z, Wu Q, Grujicic M, Wan ZY (2016) Monte Carlo simulation of grain growth and welding zones in friction stir welding of AA6082-T6. J Mater Sci 51:1882–1895

27. Zhang Z, Zhang HW (2007) Numerical studies of pre-heating time effect on temperature and material behaviors in friction stir welding process. Sci Technol Weld Join 12(5):436–448
28. Safi SV, Amirabadi H, Givi MKB, Safi SM (2016) The effect of preheating on mechanical properties of friction stir welded dissimilar joints of pure copper and AA7075 aluminum alloy sheets. Int J Adv Manuf Technol 84:2401–2411
29. Zienkiewicz OC, Taylor RL, Zhu JZ (2013) Finite element method and its basis & fundamentals, 7th edn. Elsevier, Singapore
30. Zhang Z, Zhang HW (2008) A fully coupled thermo-mechanical model of friction stir *welding*. Int J Adv Manuf Technol 37(3–4): 279–293
31. Pradeep A, Muthukumaran S (2016) Study of sub-shoulder tool wear on friction stir welded steel plates using two modes of metal transfer phenomenon. Int J Adv Manuf Technol 84:1153–1162
32. Fadaeifard F, Matori KA, Toozandehjani M, Daud AR, Ariffin MKAM, Othman NK, Gharavi F, Ramzani AH, Ostovan F (2014) Influence of rotational speed on mechanical properties of friction stir lap welded 6061-T6 Al alloy. Trans Nonferrous Metals Soc China 24(4):1004–1011
33. Sato YS, Urata M, Kokawa H (2002) Parameters controlling microstructure and hardness during friction-stir welding of precipitation-hardenable aluminum alloy 6063. Metall Mater Trans A 33(3):625–635
34. Zhang Z, Zhang HW (2007) Material behaviors and mechanical features in friction stir welding process. Int J Adv Manuf Technol 35:86–100
35. Liu G, Murr LE, Niou CS, McClure JC, Vega FR (1997) Microstructural aspects of the friction-stir welding of 6061-T6 aluminum. Scr Mater 37(3):355–361